Large amplitude l=1 coherent structures in nonneutral plasmas confined in a cylindrical trap

Ross L. Spencer and Grant W. Mason

Citation: Physics of Fluids B: Plasma Physics (1989-1993) **5**, 1738 (1993); doi: 10.1063/1.860807
View online: http://dx.doi.org/10.1063/1.860807
View Table of Contents: http://scitation.aip.org/content/aip/journal/pofb/5/6?ver=pdfcov
Published by the AIP Publishing

Large amplitude $\ell=1$ coherent structures in non-neutral plasmas confined in a cylindrical trap

Ross L. Spencer and Grant W. Mason
Department of Physics and Astronomy, Brigham Young University, Provo, Utah 84602

(Received 14 December 1992; accepted 25 February 1993)

The computation of $\ell = 1$ coherent structures in non-neutral plasmas with arbitrary density profiles and for large displacements of the plasma from the symmetry axis of a confining cylindrical trap is described. As the structures are displaced from the axis, they revolve about the symmetry axis with a frequency that typically increases with displacement. The plasma also is distorted into an approximately elliptical shape. The frequency shifts and the eccentricities as a function of displacement, plasma size, and the shape of the density profile are both computed numerically and calculated analytically. The results are shown to be consistent with data of Fine, Driscoll, and Malmberg [Phys. Rev. Lett. **63**, 2232 (1989)] which are measured for relatively large, constant-density (waterbag) plasmas ($R/a = 0.38$–0.71) and modest off-axis displacements ($D/a<0.3$). Here R is the radius of the plasma at half of peak density when centered, D is the off-axis displacement, and a is the radius of the cylinder.

I. INTRODUCTION

Consider a perfectly conducting, grounded cylinder of infinite length with radius a (see Fig. 1). External coils create a uniform longitudinal magnetic field B_0 within the volume of the cylinder. A non-neutral cold plasma of particles with charge q and density $n(r)$ is injected into the cylinder from one end to form an axisymmetric structure with a density profile that is flat or monotonically decreasing with radius. The self-field of the charge distribution creates a radial electric field which is perpendicular to the axial magnetic field, and the resulting $\mathbf{E}\times\mathbf{B}$ drift causes the plasma to rotate about the axial symmetry axis. If the density profile is flat and the density relatively low, $2\omega_p^2 \ll \omega_c^2$, the rotation frequency will be constant and is given by[1]

$$\omega_s \approx -\omega_p^2/2\omega_c = -2\pi cqn_0/B_0, \tag{1}$$

where ω_p is the plasma frequency and ω_c is the Larmor frequency. If the density profile is not flat there will be a shear in the rotational flow.

If the plasma is moved off-axis (Fig. 1), image charges are induced on the conducting boundary, giving rise to an additional radial electric field which will cause the plasma to revolve about the center of the cylindrical trap at frequency ω while continuing its spin rotation. As the plasma moves farther from the axis and approaches the wall, the frequency of the revolution increases and the shape of the plasma becomes nonlinearly more and more elliptical. Linear analysis[1] predicts, for small displacement D from the center and electric field E_w at the cylinder wall,

$$\omega \approx \omega_0 \equiv -cE_w/B_0 a. \tag{2}$$

Observations of coherent structures of the type described here have been made and reported by Fine, Driscoll, and Malmberg[2] at the University of California, San Diego. The structures are observed to revolve for up to 10^5 times. Fine *et al.* have measured the frequency shift and quadrupole moment of the plasma as a function of increasing off-axis displacement of the center-of-mass. In particular, they have made an empirical fit to the frequency-shift data,

$$(\omega-\omega_0)/\omega_0 = (D/a)^2[1.0-7.3(R/a)^6], \tag{3}$$

where R is the radius at half of peak density of the plasma.[2]

We describe here the computation of these coherent structures for arbitrary density profiles and for large displacements from the cylinder axis. Our work complements work of Prasad and Malmberg,[3] O'Neil and Smith,[4] Fine,[5] and Lund, Ramos and Davidson.[6] In Sec. II we describe the basic theory of the coherent structures within the cold-fluid, drift approximation. In Sec. III we describe a numerical algorithm for computing the structures and, in Sec. IV, we compare the results of the computation of revolution frequencies for sharp and diffuse density profiles with the empirical fit of Fine *et al.* In Sec. V we use the observation from the computational study that the potential profiles in the rotating frame are ellipses to motivate an analytic calculation that yields an approximation to both the frequencies of revolution and the eccentricities of the coherent structures as a function of size and displacement from the symmetry axis of the cylinder. In Sec. VI we compare computational, analytical, and empirical results.

II. THEORY

We describe the plasma in the cold-fluid, drift approximation in which the inertia of the particles and the temperature vanish.[1] Hence, we assume conditions in which the Larmor radius is small compared to the dimensions of the system and in which the revolution of the structures is driven by the $\mathbf{E}\times\mathbf{B}$ drift at frequencies much less than the cyclotron frequency, allowing inertial effects to be ignored. The longitudinal magnetic field B_0 is assumed uniform and

 0899-8221/93/061738-08$06.00

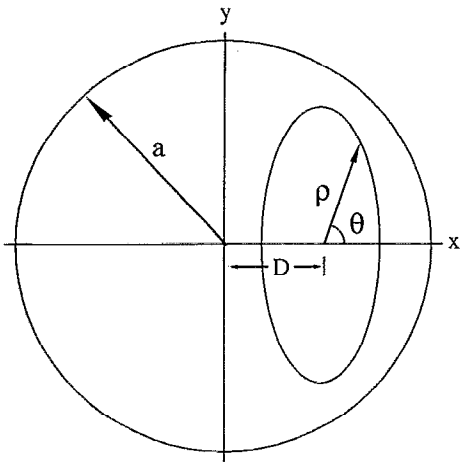

FIG. 1. A plasma of area πR^2 is bounded by $\rho(\theta)$ within a conducting cylinder of radius a. A constant, uniform magnetic field B_0 perpendicular to the plane of the diagram is created by external coils (not shown).

the bounding cylinder is considered to be a perfect conductor. We assume that the longitudinal dependence of all variables is suppressed.

In the model used here, the density is related to the electric potential through Poisson's equation,

$$\nabla^2\phi = -4\pi qn. \tag{4}$$

The fluid drift velocity is given by,

$$\mathbf{v} = -(c/B_0)\nabla\phi\times\hat{\mathbf{z}}. \tag{5}$$

For this flow $\nabla\cdot\mathbf{v}$ is identically zero, so the plasma may be taken to be an incompressible fluid. The continuity equation then becomes,

$$\frac{\partial n}{\partial t} + \mathbf{v}\cdot\nabla n = 0. \tag{6}$$

The vorticity of the plasma is given by,

$$\omega_s = \nabla\times\mathbf{v} = -4\pi qcn/B_0\hat{\mathbf{z}}. \tag{7}$$

(Levy and, more recently, Driscoll and Fine have pointed out the isomorphism between these equations and the two-dimensional Euler equations for a constant density fluid.[7–9])

The coherent structures observed by Fine *et al.* are remarkably stable, revolving many thousands of times about the symmetry axis of the cylinder before dissipating.[2] In a coordinate system which rotates with the center-of-mass, the structures can be thought of as steady states for which the time derivative of the density vanishes.

Let primed quantities be defined in the rotating frame and let unprimed quantities refer to the laboratory frame. Let ω represent the rotation frequency of the frame. Then, the electric field transforms between the frames according to

$$\mathbf{E}' = \mathbf{E} + (r\omega B_0/c)\hat{\mathbf{r}}, \tag{8}$$

i.e.,

$$\phi' = \phi - \omega B_0 r^2/2c. \tag{9}$$

Poisson's equation becomes,

$$\nabla^2\phi' = -4\pi qn - 2\omega B_0/c. \tag{10}$$

We also have,

$$\mathbf{v}' = -(c/B_0)\nabla\phi'\times\hat{\mathbf{z}}. \tag{11}$$

In the rotating frame $\partial n/\partial t = 0$, so that the continuity equation becomes,

$$\hat{\mathbf{z}}\cdot\nabla\phi'\times\nabla n = 0, \tag{12}$$

which is identically satisfied if $n = n(\phi')$.

Our computation reduces to solving Poisson's equation in the form[3]

$$\nabla^2\phi' = -4\pi qn(\phi') - 2\omega B_0/c. \tag{13}$$

III. COMPUTATIONAL ALGORITHM

The essential computational problem is the handling of the nonlinearity represented by $n(\phi')$ and ω on the right-hand side of Poisson's equation.

We begin with an axisymmetric plasma of arbitrary radial profile temporarily located at the axis of symmetry of the cylinder. In practice we have usually used profiles parametrized by the expression,

$$n(r) = n_0\frac{\tanh[-k(r^2/r_0^2-1)]+h}{\tanh(k)+h}. \tag{14}$$

This parametrization allows us to vary the profile from a flat-topped and sharp-edged profile ("waterbag") to one that has a monotonically decreasing, diffuse boundary. The parameter n_0 is the peak density, r_0 controls the position of the shoulder, $k>0$ controls the steepness of the shoulder, and $0<h\leqslant 1$ controls (somewhat) how far the plasma extends beyond r_0. The density is set to zero for larger values of r beyond the radius r_c where Eq. (14) yields negative values. In practice the area parameter R (the radius of the centered plasma measured to the point of half of peak density), h_0, and the grid spacing are specified at the beginning of the calculation. The parameters r_c, r_0, and k are then computed to ensure that negative densities are avoided and that the shoulder occurs at the correct place for the given R/a and spans at least three grid spacings. If a diffuse profile is required, k is multiplied by a fraction which has the effect of diffusing the shoulder. While this parametrization is convenient, others, including purely numerical loads, could be used.

Figures 2 and 3 show representative density profiles. Figure 2 shows a centered waterbag with a radius that is half that of the wall ($k=11.83$, $h=0.9$). Figure 3 shows a density profile of the same radius (at half of peak density), but with a diffuse profile ($k=1.479$). The plasma is shown off-axis as it appears at the conclusion of the computation. Throughout this paper we use $h=0.9$. In subsequent sections for diffuse boundaries, we have used $k=0.5260$, 1.052,2.104, respectively, for $R/a=0.125,0.250,0.500$. For sharp boundaries, we have used $k=4.208,8.417,16.83$, respectively, for $R/a=0.125,0.250,0.500$.

We distribute the density onto an $m\times m$ Cartesian grid which overlays the cylinder. The Laplacian operator is dif-

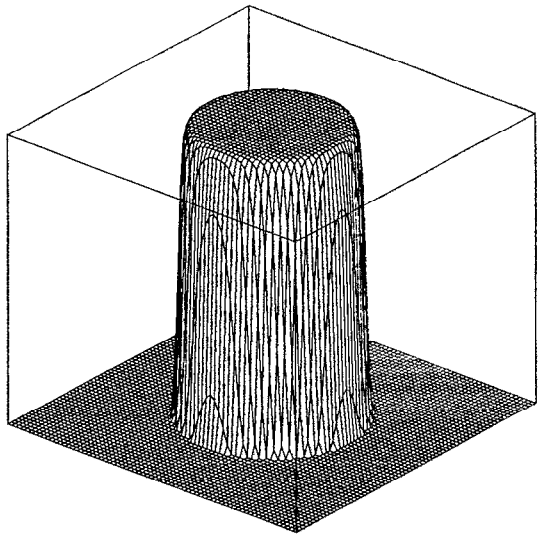

FIG. 2. Waterbag density profile shown centered. The grid size shown is 71 × 71. Shape parameters used in Eq. (14) are $h=0.9$, $k=11.83$.

ferenced with the usual five-point star except near the cylinder wall. At the edge of the cylinder, a form of the operator is constructed which uses points on the boundary.[10,11] The resulting set of equations for ϕ, representing the finite difference approximation to Poisson's equation, is solved directly with a banded-matrix solver. Typically we use $m=101$.

We are now faced with the problem that Eq. (13) has a vast number of solutions because of the freedom to choose $n(\phi')$. We make the problem mathematically more manageable, and physically more interesting, by looking

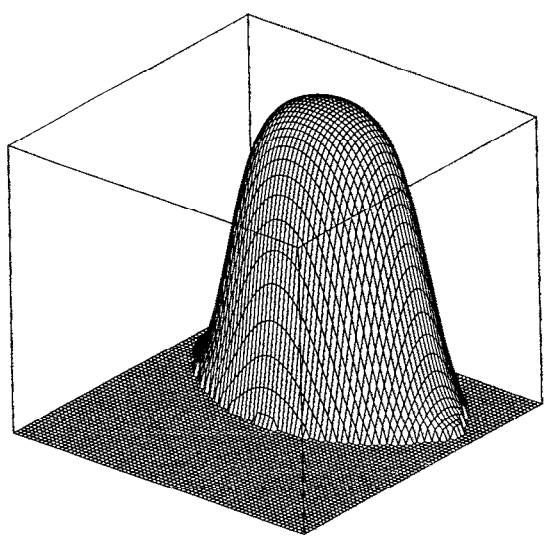

FIG. 3. Diffuse-boundary density profile shown displaced from the cylinder axis. The grid size shown is 71 × 71. Shape parameters used in Eq. (14) are $h=0.9$, $k=1.479$. Equation (14) is used to generate a centered density distribution. A numerical code then computes the distribution as it would appear if moved from a centered to an off-axis position and allowed to distort to satisfy Eq. (13).

for the off-axis states that would result from slowly displacing our initial symmetric state from the center. (Imagine, for instance, a weak instability driven by resistance in the wall.) However, the numerical code is not a time evolution code. The solution to Eq. (13) is found directly. This approach is to be contrasted with that of Lund *et al.*[6] who also connect an axisymmetric state with an off-axis, nonaxisymmetric state using a different parametrization of the problem. The connections are not the same in the two approaches.

Since the fluid is incompressible, when the centered plasma is moved off-axis and the plasma shape becomes distorted, the density contours continue to bound invariant areas A. Thus, there is a function $n(A)$ which remains invariant, and its invariance guarantees that the number of particles in the plasma is conserved. The function is computed very easily from the initial axisymmetric density load and is stored as a lookup table in the computer code.

However, Poisson's equation requires a functional relationship between n and ϕ'. We can compute such a relationship if, in addition to knowing $n(A)$, we can compute the function, $A(\phi')$. This latter function is not invariant and must be recomputed at each iterative step in the computation. In practice we define $\xi=\phi'/\phi'_{\max}$ and store $A(\xi)$ as a lookup table.

To compute an off-axis equilibrium, we choose the position at which we wish the density to be centered. We move the undistorted (and, hence, incorrect) axisymmetric density load to that position, estimate an ω for the chosen displacement and make an initial solve of Poisson's equation. We then repeat the following iterative steps until we have convergence as evidenced by a residual calculated by numerically comparing the right-hand with the left-hand side of Poisson's equation.

(1) Because the density distribution is not yet correct for the desired off-axis position, the resulting ϕ' will not be centered at the desired target position. Hence, compute a new ω which moves the peak of ϕ' radially to the desired position.

(2) Recompute $A(\xi)$ and with $n(A)$ and $A(\xi)$, compute a new density distribution for the right-hand side of Poisson's equation.

(3) Check for convergence. Stop, or, proceed to the following step.

(4) Given the density function, $n(A(\xi))$ from step (2), solve Poisson's equation for ϕ' on the grid.

(5) If the ϕ' field has slipped laterally (as opposed to radially) away from the desired displacement center, restore it by rotating the field back to the desired position.

(6) Repeat, beginning with step (1).

If necessary, one may underrelax on the iteration of ϕ' and ω, but in practice this algorithm has proved stable without underrelaxation in most instances with convergence occurring after fewer than 50 iterations. Because

$n(A)$ has been held invariant, the code conserves the number of particles. This fact is independently checked by an integration of the final density distribution.

For clarity in what follows, we will refer to results obtained from the equilibrium code described here as "computed results."

IV. COMPARISON TO THE EMPIRICAL FIT

To compare with Eq. (3), we have computed frequency shifts as a function of displacement from the cylinder axis for plasmas of different sizes and for two types of density profile.

The displacement D of the plasma from the cylinder axis is taken to be the distance from the origin to the center-of-mass. The displacements we have considered are limited by the constraint that the plasma not contact the cylinder wall. For plasmas that themselves have radii of half the wall radius, this means that the maximum value of D/a is 0.5. For thinner plasmas D/a may be larger. (It might be possible to move the plasma even closer to the wall by beginning the process of numerical convergence from an already deformed rather than circular plasma, but we have not done so, partly because of the additional complexity and partly because the present approach spans existing data.)

We have considered three plasma sizes for illustration. These are characterized by the ratio of the radius at half of peak density R to the radius of the wall a: $R/a=0.125$, 0.250,0.500. These plasmas are referred to, respectively, as "thin," "medium," and "fat."

Also for comparison, we have considered two types of density profile characterized by the parameter k in the initial density parametrization defined above. A form that closely approximates a sharp-edged waterbag results from setting $k=4.21$–16.8. A much more diffuse boundary results from setting $k=0.526$–2.10. The choice of k depends on the size of the plasma and the grid spacing as explained in Sec. III.

For a given choice of density profile and size, a series of about a half-dozen computations at different values of displacement were made and a spline fit was created which could be compared to the empirical fit of Eq. (3). The comparisons are shown in Figs. 4–6. Each figure represents a different size of plasma. The two curves in each figure are, in addition to the empirical curve, results for the waterbag profile and for the diffuse profile.

The best agreement is clearly for the larger plasma and, indeed, Fine indicates that the empirical fit arises from plasmas with R/a between 0.38 and 0.71. In our computation, $R/a=0.5$. The empirical fit does not agree with the computed curves for medium and thin plasmas, indicating a more complicated interplay between displacement and plasma radius than the form of the empirical curve allows.

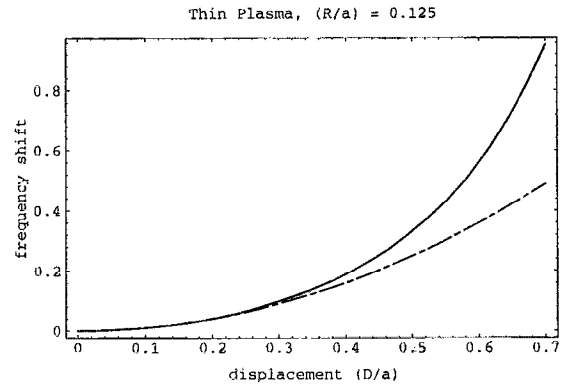

FIG. 4. Frequency shifts for a thin plasma ($R/a = 0.125$) with a sharp boundary and with a diffuse boundary compared to the empirical fit. The curves for sharp and diffuse boundaries are virtually identical (solid line) and the lowermost curve (dot-dashed) at top right is the empirical formula of Fine *et al.* The grid used is 101×101.

V. CALCULATION OF FREQUENCY SHIFTS AND ECCENTRICITIES

To calculate analytically the interplay between plasma size and off-axis displacement in determining the frequency shift and shape of the equilibria, we use the following observation from the results of the equilibrium code described above: the potential contours in the rotating frame are self-similar ellipses to very good approximation even for large displacements. This fact is established from our numerical code by comparing the ratios of the major and minor axes of the contours and by comparing the area within the contours to the area of ellipses with the same major and minor axes.

The elliptical contours are not centered at exactly the same point, but the discrepancy for different values of the potential in the region occupied by the plasma is of order 1%–2%. The discrepancy seems to be smaller for diffuse profiles (0.1%–0.2%) and larger for waterbags (1%–2%). As a measure of self-similarity, the ratio of the major

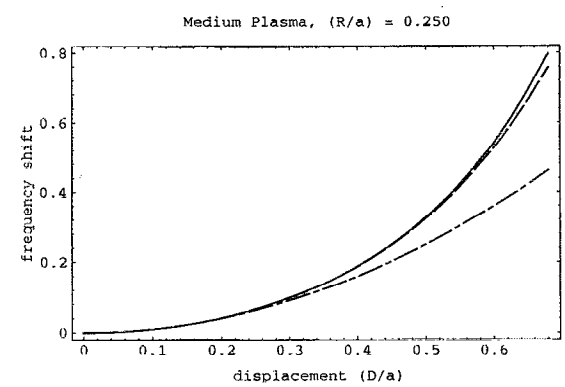

FIG. 5. Frequency shifts for a medium-size plasma ($R/a = 0.250$) with a sharp boundary and with a diffuse boundary compared to the empirical fit. The solid curve is the sharp boundary case, the dashed curve is the diffuse boundary case, and the dot-dashed curve is the empirical formula of Fine *et al.* The grid used is 101×101.

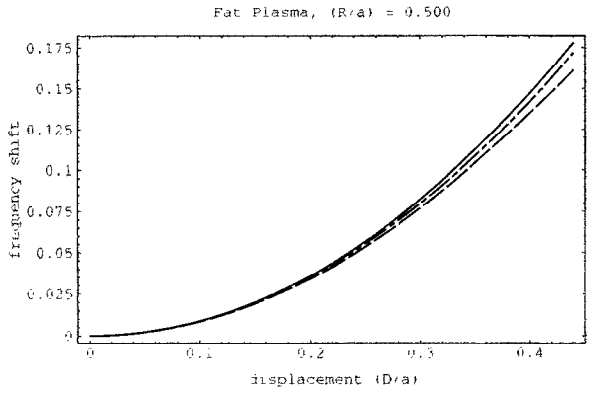

FIG. 6. Frequency shifts for a fat plasma ($R/a = 0.500$) with a sharp boundary and with a diffuse boundary compared to the empirical fit. The solid curve is the sharp boundary case. The diffuse boundary case is the dashed curve. The empirical fit curve of Fine *et al.* lies between (dot-dashed). The vertical scale is significantly reduced compared to Figs. 4 and 5 indicating a flattening of the curves as they approach the origin. As R/a increases further, both the empirical fit and our calculations predict the onset of a negative frequency shift for small D/a. The grid used is 101×101.

axis to the minor axis of the contours is the same to within 5% for potential contours within the region occupied by the plasma. In contrast to the centering, this ratio seems to be smaller for waterbags (0.5%), but larger for diffuse profiles (3%–4%).

As an approximation, then, consider an elliptically shaped distribution of density centered on the x-axis at position D (see Fig. 1). For simplicity we will take the profile to be a waterbag with uniform density $\hat{n}$ although we also present results for a diffuse (parabolic) profile. In order to make the displaced solution be dynamically connected to an axisymmetric waterbag of radius R, the area of the elliptical waterbag is required to be πR^2. The radius of the grounded cylinder is, again, a. The elliptical shape of the edge of the waterbag is given in terms of cylindrical coordinates, ρ and θ, with origin at the center of the plasma,

$$\rho^2(\theta)=\frac{R^2\sqrt{1-\epsilon^2}}{(1-\frac{1}{2}\epsilon^2)+\frac{1}{2}\epsilon^2\cos(2\theta)}, \tag{15}$$

where ϵ is the eccentricity of the ellipse. Since the problem is two dimensional, we may conveniently switch to complex variables by defining (in the laboratory frame) a source point, a field point and the electric field as,

$$z'=x'+iy', \tag{16}$$

$$z=x+iy, \tag{17}$$

and,

$$E=E_x-iE_y. \tag{18}$$

The complex-valued Green's function for the complex electric field is,[12]

$$G_E(z,z')=2\left(\frac{1}{z-z'}+\frac{1}{a^2/z'^*-z}\right). \tag{19}$$

Because of the conducting wall, there are two sources of electric field—the plasma itself and the image charges. The first term in the Green's function represents the charge of the plasma itself and the second represents the image charges.

If we integrate over the ellipse with this Green's function, we can calculate the real part of E, E_x, at $x=D$, $y=0$ from

$$E(z)=q\int G(z,z')n(z')dA'. \tag{20}$$

Letting $x=D$, we can then obtain ω from,

$$\omega=-\frac{cE_x}{xB_0}, \tag{21}$$

i.e., ω is just the $\mathbf{E}\times\mathbf{B}$ drift frequency of the center of the plasma in the laboratory frame. Note that this result will depend on the eccentricity of the ellipse which will enter as a parameter in the integration. Unfortunately, the eccentricity is not known *a priori*, but our equilibrium code tells us that in the rotating frame the contours are self-similar ellipses to good approximation. We may therefore focus our attention on the value of the eccentricity at the o-point (the center of the ellipse in Fig. 1) which marks the center of the plasma.

Near the o-point, we have in the rotating frame,

$$\begin{aligned}\phi' &\approx \phi'_0+\tfrac{1}{2}(\phi'_{xx})_0(x-x_0)^2+\tfrac{1}{2}(\phi'_{yy})_0(y-y_0)^2\\ &=\phi'_0-\frac{1}{2}\left(\frac{\partial E'_x}{\partial x}\right)_0\left(\frac{\partial E'_y}{\partial y}\right)_0\\ &\quad\times\left(\frac{(x-x_0)^2}{(\partial E'_y/\partial y)_0}+\frac{(y-y_0)^2}{(\partial E'_x/\partial x)_0}\right).\end{aligned} \tag{22}$$

By inspection the profiles, near the o-point, are ellipses with eccentricity,

$$\epsilon^2=1-\frac{(\partial E'_y/\partial y)_0}{(\partial E'_x/\partial x)_0}. \tag{23}$$

Poisson's equation in the rotating frame [Eq. (13)], the transformation of the electric field from rotating to laboratory frame [Eq. (8)], and,

$$\frac{\omega}{\omega_0}=\frac{(E_x)_0/E_w}{D/a} \tag{24}$$

[derived from Eq. (21)] may be used to obtain,

$$\epsilon^2=\frac{2(\partial E_x/\partial x)_0-4\pi q\hat{n}}{(\partial E_x/\partial x)_0-2\pi q\hat{n}(R^2/a^2)\{[(E_x)_0/E_w]/(D/a)\}}. \tag{25}$$

Here E_w is the value of the electric field at the cylinder wall when the plasma is located at the center of the cylinder with an axisymmetric profile. For a waterbag, we use Gauss' law to obtain,

$$E_w=\frac{2\pi qR^2\hat{n}}{a}. \tag{26}$$

Our problem thus reduces to using the Green's function to compute $E_x(x)$ from which we calculate $(\partial E_x/\partial x)_0$ and $(E_x)_0$ at the o-point marking the center of the plasma. We have, therefore,

$$E_x = 2q\hat{n}\int_0^{2\pi}\int_0^{\rho(\theta)}\left(\frac{1}{x-D-\rho e^{i\theta}} + \frac{(D+\rho e^{-i\theta})}{(a^2-xD-x\rho e^{-i\theta})}\right)\rho\, d\rho\, d\theta. \tag{27}$$

Because the result is only required near the o-point, we may take $x - D \ll \rho(\theta)$ and only retain terms that give a nonvanishing result for $\partial E_x/\partial x$ at $x = D$. The first term can be integrated exactly in ρ. Only the linear term in $(x-D)$ in the resulting sum need be retained for the integration over θ. The second term can also be integrated exactly in ρ, followed by an angular integration of an expansion in $x\rho(\theta)/(a^2 - xD)$. We then obtain,

$$E_x \approx 2\pi q\hat{n}a\left(\frac{x}{a}-\frac{D}{a}\right)[1+\beta(\epsilon)] + 2\pi q\hat{n}a \times\frac{(D/a)(R/a)^2}{(1-xD/a^2)} + 2\pi q\hat{n}a\sum_1^\infty (-1)^k \times\frac{(2k-1)!!}{(k+1)!}\frac{(x/a)^{2k-1}(R/a)^{2k+2}}{(1-xD/a^2)^{2k+1}}\left(\frac{\epsilon^4/4}{1-\epsilon^2}\right)^{k/2}, \tag{28}$$

where

$$\beta(\epsilon) = \frac{\frac{1}{2}\epsilon^2}{1-\frac{1}{2}\epsilon^2+\sqrt{1-\epsilon^2}}. \tag{29}$$

Defining

$$\sum_{\text{wbag}} = \sum_1^\infty (-1)^k\left(2+\frac{2k-1}{(D/a)^2}\right) \times\frac{(2k-1)!!}{(k+1)!}\frac{(D/a)^{2k}(R/a)^{2k}}{[1-(D/a)^2]^{2k}}\left(\frac{\epsilon^4/4}{1-\epsilon^2}\right)^{k/2} \tag{30}$$

we obtain

$$\frac{\omega}{\omega_0} = \frac{1}{1-(D/a)^2}+\frac{1}{(D/a)^2[1-(D/a)^2]} \times\sum_1^\infty (-1)^k\frac{(2k-1)!!}{(k+1)!} \times\frac{(D/a)^{2k}(R/a)^{2k}}{[1-(D/a)^2]^{2k}}\left(\frac{\epsilon^4/4}{1-\epsilon^2}\right)^{k/2} \tag{31}$$

and

$$\epsilon^2 = 2\left(\beta(\epsilon)+\frac{(D/a)^2(R/a)^2}{[1-(D/a)^2]^2}+\frac{(R/a)^2}{[1-(D/a)^2]^2}\sum_{\text{wbag}}\right)\Big/ 1 + \beta(\epsilon)+\frac{(D/a)^2(R/a)^2}{[1-(D/a)^2]^2}+\frac{(R/a)^2}{[1-(D/a)^2]^2} \times\sum_{\text{wbag}} -\left(\frac{R}{a}\right)^2\left(\frac{\omega}{\omega_0}\right). \tag{32}$$

These latter two expressions may be solved numerically to obtain $\omega(D/a,R/a)$ and $\epsilon(D/a,R/a)$.

Retaining only the lowest-order terms in R^2, D^2, and ϵ^2, we obtain for the waterbag,

$$\epsilon^2 \approx \frac{4(D/a)^2(R/a)^2}{[1-(D/a)^2]^2}, \tag{33}$$

$$\frac{\omega-\omega_0}{\omega_0} \approx \frac{(D/a)^2}{1-(D/a)^2}\left(1-\frac{(R/a)^4}{[1-(D/a)^2]^4}\right). \tag{34}$$

O'Neil and Smith[4] have shown that for small displacement D (and, hence, small ϵ^2), the frequency shift for waterbag profiles actually becomes negative when $(R/a)^2 > 1/2$. If we take D/a and ϵ^2 to be very small, but do not similarly restrict R/a, our analytic results reduce to

$$\epsilon^2 \approx \frac{4(D/a)^2(R/a)^2}{[1-(R/a)^2]^2} \tag{35}$$

and

$$\frac{\omega-\omega_0}{\omega_0} \approx \left(\frac{D}{a}\right)^2\left(1-\frac{(R/a)^4}{[1-(R/a)^2]^2}\right). \tag{36}$$

From the latter expression we observe that the frequency shift becomes negative when $(R/a)^2 > 1/2$, i.e., $R/a > 0.707$. This value of R/a agrees with the result of O'Neil and Smith and the approximate value implied by Eq. (3). We also observe this threshold ($R/a \approx 0.702$ for $D/a = 0.04$) with the numerical code using the waterbag approximation described in Sec. III.

If the density is given a diffuse parabolic profile with a cutoff at $r = R_c$,

$$n(r) = n_0[1-(r/R_c)^2], \tag{37}$$

we may repeat the calculation. The radius at half of peak density R is related to R_c by $R = R_c/\sqrt{2}$. Defining,

$$\sum_{\text{par}} = \sum_1^\infty (-1)^k\left(2+\frac{2k-1}{(D/a)^2}\right) \times\frac{(2k-1)!!}{(k+2)!}\frac{(D/a)^{2k}(R_c/a)^{2k}}{[1-(D/a)^2]^{2k}}\left(\frac{\epsilon^4/4}{1-\epsilon^2}\right)^{k/2} \tag{38}$$

we obtain

$$\frac{\omega}{\omega_0}=\frac{1}{1-(D/a)^2}+\frac{2}{(D/a)^2[1-(D/a)^2]}\times\sum_1^\infty(-1)^k\frac{(2k-1)!!}{(k+2)!}\times\frac{(D/a)^{2k}(R_c/a)^{2k}}{[1-(D/a)^2]^{2k}}\left(\frac{\epsilon^4/4}{1-\epsilon^2}\right)^{k/2} \tag{39}$$

and

$$\epsilon^2=2\left(\beta(\epsilon)+\frac{1}{2}\frac{(D/a)^2(R_c/a)^2}{[1-(D/a)^2]^2}+\frac{(R_c/a)^2}{[1-(D/a)^2]^2}\sum_{\text{par}}\right)\Big/1+\beta(\epsilon)+\frac{1}{2}\frac{(D/a)^2(R_c/a)^2}{[1-(D/a)^2]^2}+\frac{(R_c/a)^2}{[1-(D/a)^2]^2}\times\sum_{\text{par}}-\left(\frac{R_c}{a}\right)^2\left(\frac{\omega}{\omega_0}\right). \tag{40}$$

Reverting to the use of R rather than R_c to facilitate comparison with the waterbag case, we have, to lowest order,

$$\epsilon^2\approx\frac{4(D/a)^2(R/a)^2}{[1-(D/a)^2]^2}, \tag{41}$$

$$\frac{\omega-\omega_0}{\omega_0}\approx\frac{(D/a)^2}{1-(D/a)^2}\left(1-\frac{4}{3}\frac{(R/a)^4}{[1-(D/a)^2]^4}\right). \tag{42}$$

Note that the eccentricity formula for the waterbag [Eq. (33)] is the same as the formula for the parabolic profile [Eq. (41)]. However, the frequency shift formulas [Eq. (34) and Eq. (42)] differ.

We observe that for the parabolic density profile there is also a threshold in plasma size above which the frequency shift is negative. For D/a and ϵ^2 small, but R/a not restricted, our results for the parabolic profile reduce to

$$\epsilon^2\approx\frac{4(D/a)^2(R/a)^2}{1-4(R/a)^2+(4/3)(R/a)^4} \tag{43}$$

and

$$\frac{\omega-\omega_0}{\omega_0}\approx\left(\frac{D}{a}\right)^2\left(1-\frac{4}{3}\frac{(R/a)^4}{[1-4(R/a)^2+(4/3)(R/a)^4]}\right). \tag{44}$$

Thus, for the diffuse parabolic profile, the reversal in the sign of the frequency shift occurs when $R/a > 0.500$, i.e., $R_c/a > 0.707$.

While the lowest-order expressions for either waterbag or parabolic profiles result in separate formulas for ω/ω_0 and ϵ^2, in general one must resort to a numerical technique to solve for ϵ^2. For clarity, however, in comparing these results with those obtained from our equilibrium code ("computed results"), we will refer to all results from this section as "analytic results."

VI. COMPARISON OF ANALYTIC AND COMPUTED FREQUENCY SHIFTS

We now compare computed and analytic frequency shifts for a waterbag profile in the thin and medium sizes shown in Figs. 4 and 5, i.e., for $R/a=0.125,0.250$. In these instances we use the lowest-order expressions [Eqs. (33) and (34)] obtained in Sec. V for the waterbag case. In the case of $R/a=0.125$, a plot of the lowest-order approximation to the frequency shift as a function of displacement [Eq. (34)] is indistinguishable from the plot of computed shifts in Fig. 4. Only a slight difference between the lowest-order analytic result of Eq. (34) and the computed frequency shifts is apparent for $R/a=0.250$ as seen in Fig. 7. The empirical expression of Fine *et al.* is also shown for comparison.

As the size of the plasma increases, the discrepancy between our computed and our lowest-order analytic results grows, meaning that higher-order terms in the analytic expressions become more and more important. In Fig. 8 we make the same kind of comparison as in Fig. 7, but we use the full sums [Eqs. (31) and (32)] and use a zero-

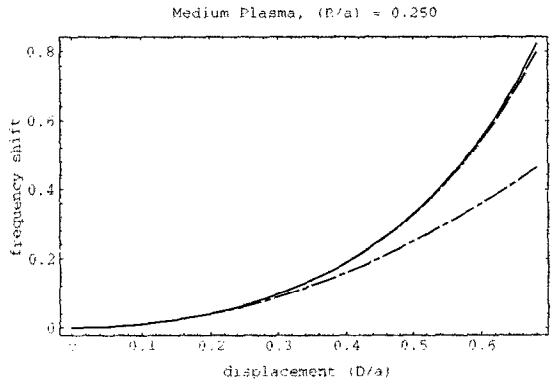

FIG. 7. Analytic frequency shifts from Eq. (34) compared to computed shifts for the waterbag profile with $R/a = 0.250$ used in Fig. 5. The analytic result (solid) differs slightly from the computed result (dashed). The lower curve (dot-dashed) is the empirical-fit curve of Fine *et al.* The lowest-order approximation to the analytic result is used.

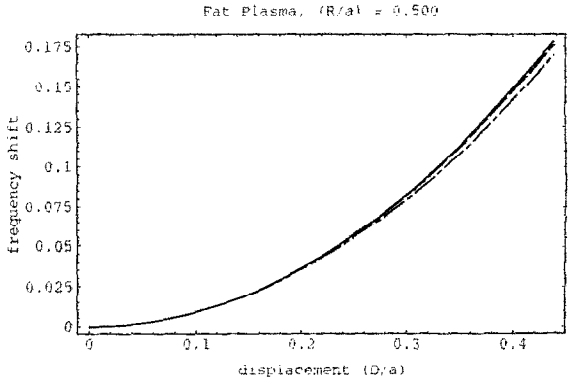

FIG. 8. Analytic frequency shifts from Eqs. (31) and (32) compared to computed shifts for the waterbag profile with $R/a = 0.500$ used in Fig. 6. The analytic result (solid) and computed result (dashed) are nearly indistinguishable in the curve at top, right. The lower curve (dot-dashed) is the empirical-fit curve of Fine *et al.* Higher-order terms are included in the analytic result. The vertical scale is significantly reduced as in Fig. 6. As R/a increases, both the empirical fit and theory predict the onset of a negative frequency shift for small D/a.

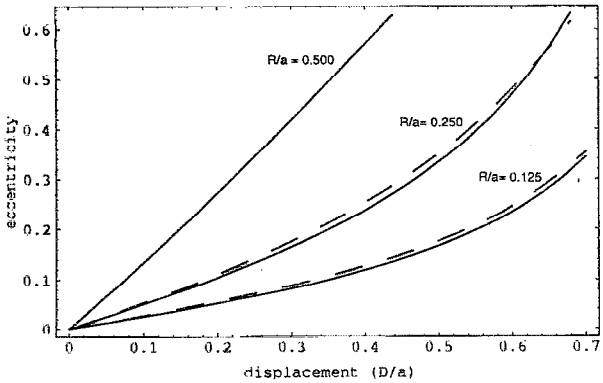

FIG. 9. Comparison of analytic eccentricities (solid line) and computed eccentricities (dashed line) for the waterbag profiles of Figs. 4–6. The lowest-order approximation [Eq. (33)] is used to obtain the analytic curves for R/a=0.125,0.250. Higher-order terms in Eqs. (31) and (32) are used to obtain the analytic curve for R/a=0.500 which is identical to the computed curve for the waterbag case in Fig. 6. If higher-order terms are used for R/a=0.125 and 0.250, the discrepancy between the analytic and computed curves disappears for R/a=0.250 and narrows slightly for R/a=0.125.

finding technique to solve for ϵ^2. As Fig. 8 shows, we restore nearly full agreement between our computed and our analytic results.

We can also compare the analytic and computed values for plasma eccentricities (see Fig. 9). Again, the cases shown are for R/a=0.125,0.250,0.500. For the thin and medium sizes we use the lowest-order approximation of Eq. (33). For R/a=0.500 we use the full sums and a zero-finding technique to find ϵ^2 from Eqs. (31) and (32).

VII. CONCLUSION

We have used finite difference methods on a square grid to compute frequency shifts and elliptical distortions of coherent structures in non-neutral plasmas confined off-axis in a cylindrical trap by a uniform, axial magnetic field. We have used a cold plasma, drift approximation model. The frequency shifts are shown to depend in a complicated way both on the displacement of the plasma from the cylinder center as well as on the size of the plasma. The predicted frequency shifts from our finite difference calculation agree well with an empirical fit to data of Fine *et al.* when applied to plasmas for which $D/a \approx 0.5$ (the regime from which the data are taken). An analytic result based on experience gained from the numerical code is shown to agree closely with our numerical results as well as with the empirical fit of Fine *et al.* in the appropriate parameter regime. The numerical code works as well for arbitrary diffuse profiles as for step-function profiles (waterbags) while the analytic theory is tractable for at least some choices of diffuse profile.

[1]R. C. Davidson, *Physics of Nonneutral Plasmas* (Addison–Wesley, Redwood City, CA, 1990), Chap. 6.
[2]K. S. Fine, C. F. Driscoll, and J. H. Malmberg, Phys. Rev. Lett. **63**, 2232 (1989).
[3]S. A. Prasad and J. H. Malmberg, Phys. Fluids B **29**, 2196 (1986).
[4]T. M. O'Neil and R. A. Smith, Phys. Fluids B **4**, 2720 (1992).
[5]K. S. Fine, Phys. Fluids B **4**, 3981 (1992).
[6]S. M. Lund, J. J. Ramos, and R. C. Davidson, Phys. Fluids B **5**, 19 (1993).
[7]C. F. Driscoll and K. S. Fine, Phys. Fluids B **2**, 1359 (1990).
[8]R. H. Levy, Phys. Fluids **8**, 1288 (1965); **11**, 920 (1968).
[9]R. J. Briggs, J. D. Daugherty, and R. H. Levy, Phys. Fluids **13**, 421 (1970).
[10]R. L. Spencer, Phys. Fluids B **2**, 2306 (1990).
[11]G. D. Smith, *Numerical Solutions of Partial Differential Equations* (Oxford University Press, London, 1965), p. 139.
[12]W. R. Smythe, *Static and Dynamic Electricity* (McGraw-Hill, New York, 1939), Chap. 4.